On the high resolution coastal applications with WAVEWATCH III®

14^{th} International Workshop on Wave Hindcasting and Forecasting, and 5^{th} Coastal Hazard Symposium

Key West, Florida, USA, Nov 8-13, 2015.

Marion Huchet,
Service Hydrographique et Océanographique de la Marine, Brest, France
École Centrale Nantes, Nantes, France

Fabien Leckler,
Service Hydrographique et Océanographique de la Marine, Brest, France

Jean-François Filipot,
France Énergies Marines, Plouzané, France

Aron Roland,
BGS IT&E, Darmstadt, Germany

Fabrice Ardhuin,
Laboratoire de Physique des Océans, UMR 6523 CNRS-IFREMER-IRD-UBO, 29200 Plouzané, France

Mathieu Dutour Sikirić,
Institute Ruder Bosković, Zagreb, Croatia

Héloïse Michaud,
Service Hydrographique et Océanographique de la Marine, Brest, France

Matthias T. Delpey,
SUEZ Eau France - Rivages Pro Tech, Bidart, France

Guillaume Dodet,
GEOMER - UMR 6554, CNRS-LETG, Institut Universitaire Européen de la Mer, Plouzané, France

1 Introduction

Phase-averaged wave models consider the spectral decomposition of sea surface elevation across wavenumbers k (or frequencies f) and directions θ at point (x, y) and time t. The evolution of spectral density $F(k, \theta, x, y, t)$ is resolved using the wave energy equation [Gelci et al., 1957]:

$$\frac{\mathrm{d}F}{\mathrm{d}t} = S_{\mathrm{atm}} + S_{\mathrm{nl}} + S_{\mathrm{wcap}} + S_{\mathrm{bt}} + S_{\mathrm{br}} + ... \qquad (1)$$

where the Lagrangian derivative of spectral density, on the left-hand side, includes the local time evolution and advection in both physical and spectral spaces [e.g. WISE Group, 2007]. The first source term on the right-hand side is the atmospheric source term S_{atm}, which includes the classical input of energy S_{in} from wind to wave and the energy S_{out} from waves to wind[1], associated with friction at air-sea interface [Ardhuin et al., 2009]. The nonlinear source term S_{nl} represents energy transfers in the spectral domain due to wave-wave interactions. S_{bt} is the sink of energy due to bottom friction. S_{br} represents the strong depth-induced wave breaking process on the shore. S_{wcap} describes the wave dissipation due to white-capping; other effects may also be included such as Bragg-scattering [see e.g. WISE Group, 2007].

With the implementation of unstructured grids e.g. [Benoit et al., 1996, Roland et al., 2005, Roland, 2008], spectral wave models became appropriate tools

[1] The transfer of energy from waves to wind (S_{out}) is responsible for the swell dissipation over long distances. A modification of the Ardhuin et al. [2010]'s formulation was provided by Leckler et al. [2013].

for sea state modeling in coastal areas. In particular, recent developments in WAVEWATCH III®[Tolman et al., 2014, hereinafter WW3] included the wave setup process, wave breaking and triad interactions for better wave modeling in coastal areas. Nevertheless, the increasing need of very high resolution grids also brings up the problem of the limited computational resources for many operational applications. Simulations on such high resolution grids are not solvable at all with explicit methods, due to the small time step imposed by the Courant–Friedrichs–Lewy (CFL) criteria. Therefore we have introduced into WW3 the numerical concept that was successfully implemented in WWM-III [Roland et al., 2012, Roland and Ardhuin, 2014].

2 Model developments

We present here the validation of the new numerical schemes within the WW3 framework. We have parallelized the currently available unstructured grid (hereinafter UG), using domain decomposition methods and a new implicit scheme that is 1st order in time and space. The new scheme resembles the famous SIMPLE algorithm [Patankar, 1980] which is widely used for the integration of the Navier-Stokes equations. The left-hand side of the equation is integrated using 1st order numerical schemes in time and space, where in space the residual distribution framework in terms of the N-Scheme has been introduced. The right hand side of the equation uses the same integrator as in WW3 but in matrix form. It writes the functional derivate of the source terms after dropping the off-diagonal contributions and it linearizes them on the diagonal of the matrix using Patankar rules. This way, negative parts are integrated on the new time level, which strengthens the diagonal part of the matrix and improves convergence behavior of the linear solver. We also linearize the source terms within the integration time step; however, since the spectral balance in deep water needs a limiter to ensure stable integration, we have splitted the integration of the source terms so as not to limit the solution of the negative shallow water source terms. For these, fully non-linear integration is also available within the iterative solver. The latter option is still under development. The most important thing in the integration scheme is that the limiter is not acting on spatial advection, and therefore it ensures that the transient modes are well represented according to the order of the scheme itself. This new numerical methods obey no splitting error contrary to the former schemes on structured and unstructured grids. They give time-independent, steady-state solutions and can be used with reasonable large time steps to integrate WAE oscillation free in time.

3 Model Verification

As the model and the numerics have just been developed, we present in this paper the 1st tests on accuracy and efficiency of the newly developed methods. We start with the usual testcase for wave growth and then look into shoaling/refraction. Then, in order to test the advection term in frequency-direction space, we look at following and opposing currents. To combine propagation effects and evaluate the various schemes, we picked the Vincent & Briggs case that involves focusing over an elliptical shoal. We validate the strong non-linear wave breaking source term on a linear sloping beach, where we investigate time step dependency of the solution and various effects of the limiters in WW3. Last but not least, we investigate the effects of wave approaching strongly under-resolved step-bathymetries and islands, where e.g. the SWAN model was reported to blow up due to so called inaccuracies [see e.g. Dietrich et al., 2013] and needed to apply limiters to retain a stable integration which, however, resulted in significant differences in the solutions [Roland and Ardhuin, 2014].

3.1 Case 1 : Wave growing under constant wind

Blowing over the sea, the wind transfers energy to the waves with a phase speed lower than wind speed, whereas the waves with a phase speed lower than wind speed dissipate energy by air-sea friction [Ardhuin et al., 2010]. In the same time, a part of this energy dissipates with wave breaking. Another part of this energy is redistributed in the wave spectrum with non-linear interactions. In the spectral wave model, these processes are respectively represented by the source terms S_{atm}, S_{wcap} and S_{nl} in the wave energy balance equation (1). The source term parametrization here tested is the parameterization TEST451 of Ardhuin et al. [2010] including the correction for the swell dissipation of Leckler et al. [2013].

Here we consider source terms integration performed on a small unstructured grid, corresponding to uniform deep ocean conditions. The infinite ocean is modeled by deactivating the wave energy advection in space. The wave energy advection in spectral domain is also disabled for computational cost considerations, because of the uniform depth and the absence of current. The wave energy balance (1) is then reduced to:

$$\frac{\partial F}{\partial t} = S_{\mathrm{atm}} + S_{\mathrm{nl}} + S_{\mathrm{wcap}}. \tag{2}$$

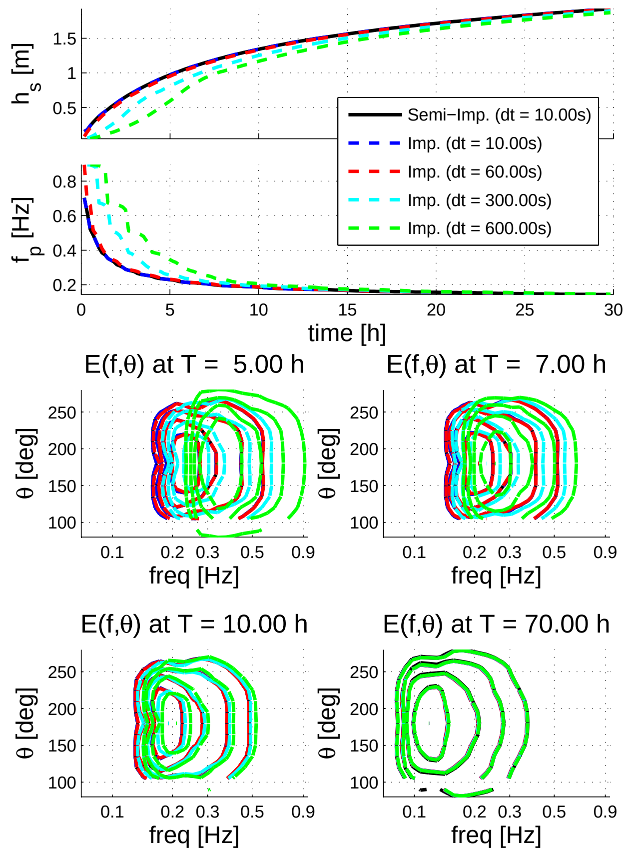

Figure 1: Top panels : Time series of the significant wave height, H_{sig} (top) and of peak frequency, f_{p} (bottom). Bottom panels : Shapes of the extracted spectra after 5, 7, 10 and 70 hours of integration. The wind speed is constant to 10 m/s.

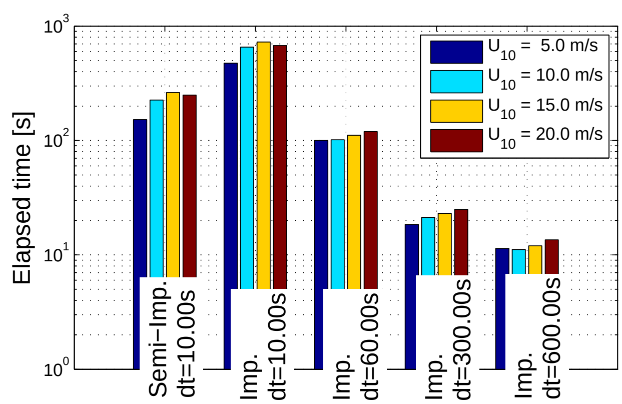

Figure 2: Comparison of the computational times with the different schemes and with the different time steps. The shown computational times are extracted from the model log file and correspond to a single processor run.

The equation is integrated for 72 hours and the wave evolution is started from rest with constant winds, U_{10}, of 5, 10, 15 and 20 m.s^{-1}. The wave growth and the non-linear frequency shifthing obtained with $U_{10} = 10$ m.s^{-1} are shown in the figure 1 (top panels), using both the "historical" semi-implicit scheme and the newly implemented implicit scheme. The shape of the obtained spectra after 5, 7, 10 and 70 hours of integration are plotted on the bottom panels. Both schemes provide a nearly perfect fit up to numerical errors using the same time step d$t = 10$ s (in the figure, the last plotted curve recovers previous ones). Increasing the time step with a factor 6, the semi-implicit scheme (not plotted here) provides a clearly slower wave growth, whereas the implicit scheme keeps in line. The computational times for both schemes are also investigated and are shown in figure 2. The computational times are extracted from the model log file and correspond to a single processor run. Typically, for the same time step the semi-implicit scheme is faster by a factor 2 to 3 than the implicit scheme. The advantage of the implicit scheme comes with the increase in the time step, which strongly reduces the computational cost while keeping appropriate results. The dependence of the computational cost for both schemes is caused by the increasing number of iterations needed to make the results convergent.

3.2 Case 2 : Wave-current interactions

When propagating in a non-uniform current, the wave spectrum is affected by the energy advection occurring in spectral space. A current collinear to the wave propagation induces a frequency shifting, whereas a cross current implies wave refraction. For the wave-current interaction test cases, we consider a 226-node unstructured grid covering an area with longitudes from 0 degree to 0.072 degree and with latitudes from 0 degree to 0.036 degree.

Moreover, the model was integrated using various explicit schemes: a first order scheme given by the switch PR1 and a third order scheme provided by the switches PR3 and UG (instead of PR1). The explicit schemes are here all used with the EXPFSN scheme.

We first consider waves going along an increasing current, to disable the effect of the breaking occuring when waves face an increasing current. The ocean depth is uniform ($d = 5000$ m) over the considered area. A South-North current linearly increases from $U_{\text{cur}} = 0$ m.s^{-1} at the latitude 0 deg to $U_{\text{cur}} = 2$m.s^{-1} at latitude 0.036 deg and is constant along longitudes and in time. The waves are forced at the southern boundary, where the current is null. The input wave spectrum is created using WW3 pre-processing tools *ww3_ strt* and is constant in time. The forced boundary wave spectrum is gaussian in frequency and cosinus type in direction. The peak frequency is defined to $f_\mathrm{p} = 0.1$ Hz with a frequency spread of 0.01 Hz. The wave mean direction is defined to $\theta_m = 270$ deg in oceanographic convention (from South to North, so that waves propagate with the increasing current) with a spreading defined by a cosine power equal to 20. As a result, the boundary spectrum is very narrow in frequencies and directions. The figure 4 compares the profiles obtained after 20 hours of integration for the explicit schemes [PR3 UG,EXPFSN and PR1,EXPFSN] and the newly coded implicit scheme. From top to bottom, the profiles are respectively the current speed profile U_cur, the significant wave height $H_\mathrm{sig} = 4\sqrt{E}$, the mean wave length $L_\mathrm{m} = 2\pi\overline{k^{-1}}$, the mean wave period, $T_{m\ 0,2} = 2\pi/\sqrt{\overline{\sigma^2}}$, the mean wave period, $T_{m0,-1} = 2\pi\overline{\sigma^{-1}}$, the peak frequency, f_p, and the mean wave direction $\theta_m = \mathrm{atan}\left(\frac{b}{a}\right)$, with $a = \int_0^{2\pi}\int_0^{\infty}\cos(\theta)F(\sigma,\theta)\mathrm{d}\sigma\mathrm{d}\theta$ and $b = \int_0^{2\pi}\int_0^{\infty}\sin(\theta)F(\sigma,\theta)\mathrm{d}\sigma\mathrm{d}\theta$. As the implicit scheme must be of first order, the fit is obtained with the first order explicit scheme. As expected, the higher order scheme provides slightly different results, expected to be more in line with the physics. Increasing the time step, both schemes diverge from lower time step resolved results. This is not expected using the implicit scheme. However, the results are only a bit different and we think that the reason for this difference is the way we are handling the high frequency part of the spectra, which must be further investigated.

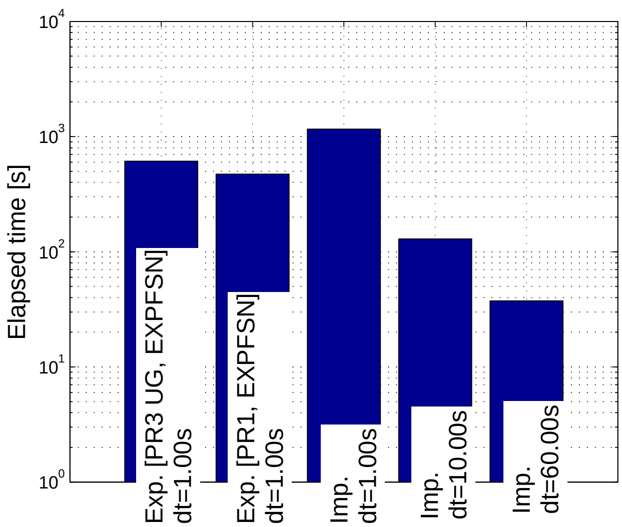

Figure 3: Comparison of the computational times with the different schemes and with the different time steps. The shown computational times are extracted from the model log file and correspond to a MPI 8-processor run.

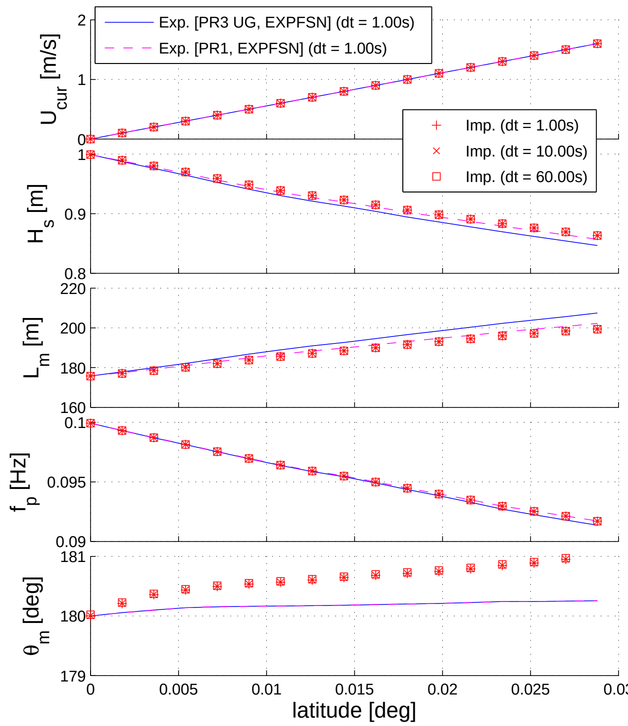

Figure 4: Comparison of the profiles obtained after 20 hours of integration for the explicit and implicit schemes with different time steps for the waves propagating without incidence in the increasing current.

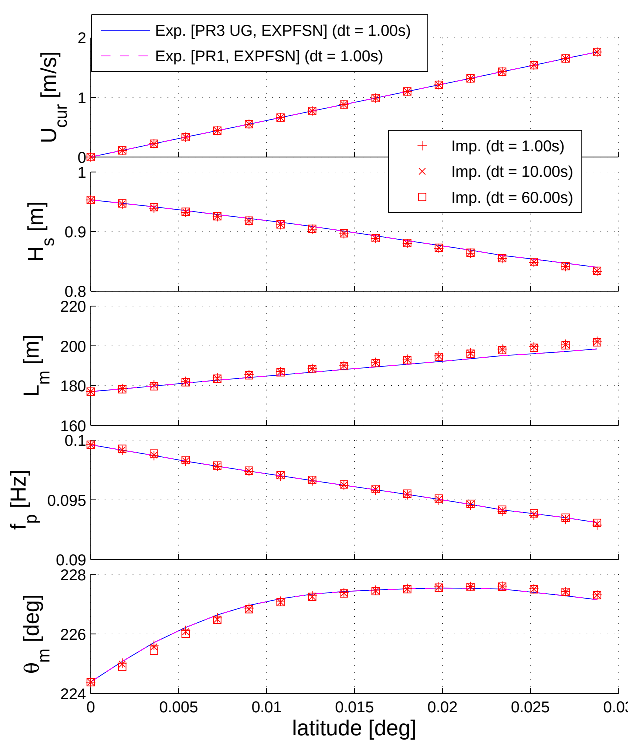

Figure 5: Comparison of the profiles obtained after 20 hours of integration for the explicit and implicit schemes with different time steps for the waves propagating with incidence in the increasing current.

On the other hand, we implemented a configuration with waves going with an increasing cross current. Here the South-North current linearly increases from $U_{\text{cur}} = 0$ deg on the Eastern and Southern boundaries to $U_{\text{cur}} = 4$ m.s^{-1} at longitude 0.070 deg and latitude 0.035 deg (North-West corner of our area). The waves are now forced at the Eastern and Southern boundaries, where the current is null. The input wave spectrum is again created using WW3 pre-processing tools *ww3_strt* with the same definitions as previously, except for the wave mean direction which is now defined to $\theta_m = 235$ deg (in oceanographic convention, from South-East to North-West) so that waves propagate in the increasing South-North current with a non-null incidence. This non-null incidence implies the refraction of the waves. Figure 5 shows the profiles obtained after 20 hours of integration for both explicit and implicit schemes, as described above. The conclusions for this test case are similar to the previous one: a fit is obtained with the first order explicit scheme, validating the implicit refraction scheme, but providing slightly worse results than higher order schemes. Clearly, more investigation is needed for this case.

3.3 Case 3 : Wave reaching coast over a linear beach

The profile of the linear beach is a constant slope of 1:25 on Y-axis. The profile length is 300m, from $Y = 0$ m with $z = 0$ m to $Y = 300$ m with $z = -12$ m. The profile is constant along X-axis and the beach width is 1000 m from $X = -500$ m to $X = 500$ m. A rectilinear grid with a resolution defined to d$X = 10$ m (along-shore) and d$Y = 5$ m (cross-shore) is implemented. Then, by cutting the rectangles of the rectilinear grid in their diagonal, we create the triangular grid. The waves are forced at the $Y = 300$ m boundary with a JONSWAP spectrum. Two input spectra are created with the significant wave height chosen to $H_{\text{sig}} = 0.5$ m and the peak frequency to $f_{\text{p}} = 0.20$ Hz. The model is integrated for 3 minutes.

First, we consider waves propagating without any incidence angle over the beach. The profiles obtained at the center of the beach are plotted in figure 6 with both explicit and implicit schemes. The explicit scheme is run with time steps d$t = 0.05$ s corresponding to CFL<1. The implicit scheme is run with the same time step and with time steps increased by factors up to 100 (i.e. d$t = 5$ s). The explicit time step for the source terms integration is chosen small enough to well resolve the bathymetric breaking dissipation without any need of the Miche Limiter (switch MLIM in WW3), which is then deactivated for all configurations. Moreover, the model was integrating using various explicit schemes, with both a first order scheme given by the switch PR1 and a third order scheme provided by the switches PR3 and UG (instead of PR1). The explicit schemes are here all used with the EXPFSN scheme. The results obtained with the implicit scheme well fit those obtained with the first order explicit scheme [PR1, EXPFSN] on the unstructred grid; they are in line with the profiles obtained with the third order scheme [PR3 UG, EXPFSN].

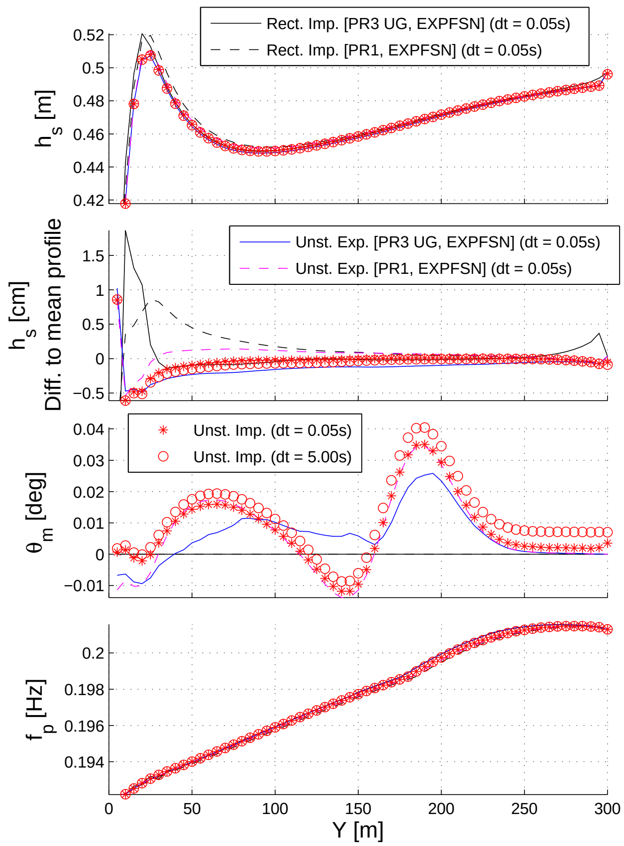

Figure 6: Cross-shore profiles obtained after 3 minutes of integration. The profiles are extracted at the center of the beach ($X = 0$ m) to avoid edge effects. The mean wave direction of propagation at the open boundary is perpendicular to the beach isobathes. From top to bottom, the first panel shows the significant wave height (H_s) profiles, the second one is the difference of each H_s profile to the mean H_s profile (meaning over all schemes). Then, the third panel represents the mean wave direction, and finally, the last one shows the peak frequency profiles.

We then consider waves propagating with a non-null incidence angle over the beach. The input boundary JONSWAP spectrum is now defined to provide an angle of 25° between wave propagation and cross-shore axis. The depth gradient along wave crest then leads to wave refraction. The refraction of waves is plotted on the bottom profiles of figure 7. This case also shows the same conclusion, with a quite perfect fit of the wave refraction obtained between the implicit and the explicit first order scheme [PR1, EXPFSN] on the unstructured grid.

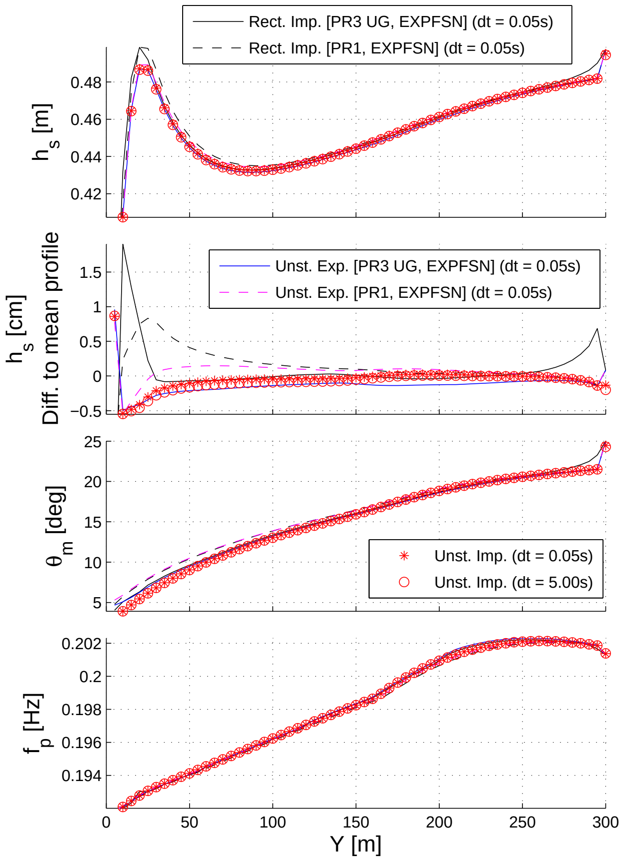

Figure 7: Cross-shore profiles obtained from the grid after 3 minutes of integration. The profiles are extracted at the center of the beach ($X = 0$ m) to avoid for the edge effects. The mean wave propagation at the open boundary is here forced with a non-null incidence angle of 25 deg. From top to bottom, the first panel shows the significant wave height (H_s) profiles, the second one is the difference of each H_s profile to the mean H_s profile (meaning over all schemes). Then, the third panels represents the mean wave direction, and finally, the last one shows the peak frequency profiles.

3.4 Case 4 : The Deep Sea Island case

The next case is inspired by the paper of Dietrich et al. [2013] to show that we have for such a case monotone and stable results in our numerical model, in contrast to the results shown in the latter work. The intention of this test is rather to show the model convergence and stability in regions of under-resolved bathymetry. There is one island defined as a hole in the mesh and the others are submerged, going from 1000m depth to 10m and 15m respectively (see figure 8). The results are fully convergent up to a solver threshold of 10E-20, stable and monotone (see figure 9), which is expected from a 1st order monotone implicit scheme. However, more tests are needed to have more evidence with respect to the robustness of the numerical scheme. The boundary of the island represented by a hole in the mesh does not take spectra propagation into account, which increases convergence speed. If the island is further resolved refraction effects come naturally. However, we would like to stress again that no limiters are used neither on slope nor on propagation speeds. The scheme developed here is a building block for higher order schemes, which is the basis and must be consistent.

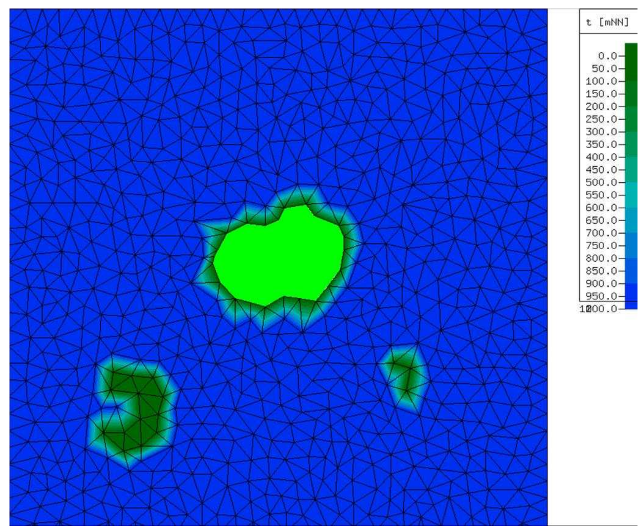

Figure 8: Bathymetry of the Deep Sea Island.

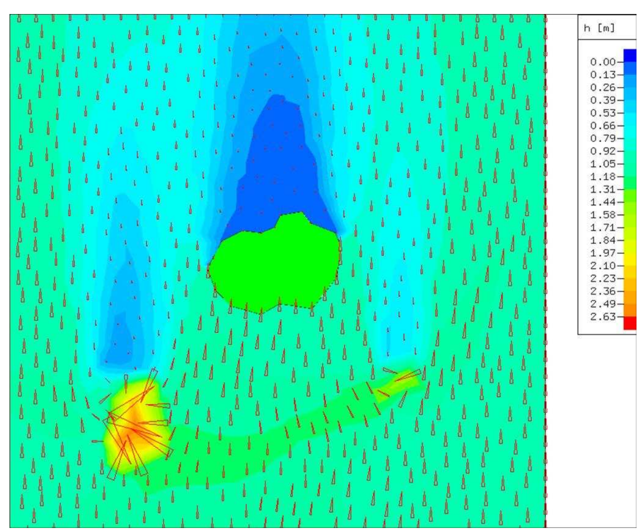

Figure 9: Results for the Deep Sea Island case

3.5 Case 5 : Waves over an elliptic mount

The next case is inspired by the tank experiment of Vincent and Briggs [1989] with the motivation to compare the refraction/shoaling characteristics of the various schemes, as well as to investigate time step dependency of the new developed model. In our simulations, water depth is set at a constant value outside the elliptic shoal. The bathymetry is shown in figure 10 with the dashed lines representing the profiles investigated in this paper.

The elliptic shoal is patterned with a major radius of 4 m along Y, a minor radius of 3 m along X and a maximum height of $h_{\max} = 30.48$ cm at the center. Outside the ellipse, the water depth is equal to $d_{\max} = 45.72$ cm. Therefore, at the top of the ellipse the water depth reaches a minimum equal to $d_{\min} = 15.24$ cm. The perimeter of the elliptic shoal is then defined with:

$$\left(\frac{X}{3}\right)^2 + \left(\frac{Y}{4}\right)^2 = 1. \quad (3)$$

The depth d is defined in the perimeter with:

$$d(X,Y) = d_{\max} + h_{\max} * \sqrt{1 - (\frac{X'}{3})^2 - (\frac{Y'}{4})^2} \quad (4)$$

and with $d(X,Y) = d_{\max}$ else.

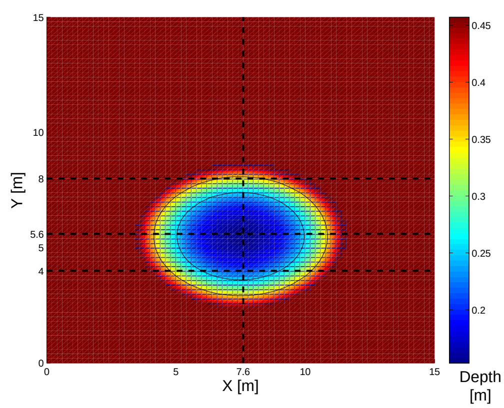

Figure 10: Bathymetry inspired of the elliptic mount experiment of Vincent and Briggs [1989].

Three meshes were created. The first mesh is a rectilinear grid with resolution $dX = dY = 0.2$ m. The second mesh is triangular and is formed by cutting squares of the rectilinear grid in their diagonal to create the triangles. The third mesh is a 2571-node unstructured mesh created with non-regular triangles. The results obtained with the two unstructered grids are very similar and here we only present the results obtained with the non-regular, triangular mesh. The input spectra are forced on all boundaries. All the possible explicit schemes implemented in WW3 are tested here, following Roland [2008]. These schemes are implemented in WW3 following the concept of the fractional step method and are either mixed with 1st order upwind schemes or with 3rd order Ultimate Quickest schemes for spectral space. The implicit scheme is entirely 1st order in time and space.

Four cases are experimented in this study, corresponding to the tests 02, 03, 16 and 17 of Vincent and Briggs [1989]. We keep their test numbers in this paper. The two first cases (TEST02 and TEST03) correspond to non-breaking cases, with respectively narrow (figure 11) and broad (figure 12) input spectra. The two next cases (TEST16 and TEST17) correspond to breaking cases, with respectively broad (figure 13) and narrow (figure 14) input spectra.

The explicit scheme is run with both first and third order schemes, with the time step defined as $dt = 0.01$ s (CFL<1) on a rectangular grid. The 3rd order solution can be seen as a reference solution. The explicit schemes up to 2nd order in time and space result in under- and overshooting of the 3rd order results, but the 1st order results either implicit or explicit are more or less in line with the explicit results. It seems that the implicit scheme is a bit more diffusive than the explicit fluctional splitting schemes. The implicit scheme is run with the same time step and aslo with the time step increased by a factor 100. We first notice that the two implicit runs provide very similar results, with a computational time step reduced by a factor more than 30 for the larger time step and for all cases. The results for the higher order schemes of WW3 are somewhat suspicious in terms of overshooting to the 3rd order Ultimate Quickest, which needs further investigation. Moreover, we need to take into account higher order propagation effects as discussed in e.g. Holthuijsen et al. [2003], Toledo et al. [2012], Liau et al. [2011]. However, this includes amplitude dispersion that makes the left-hand side fully nonlinear, since the wave velocities depend on various spatial and temporal gradients of the solution itself.

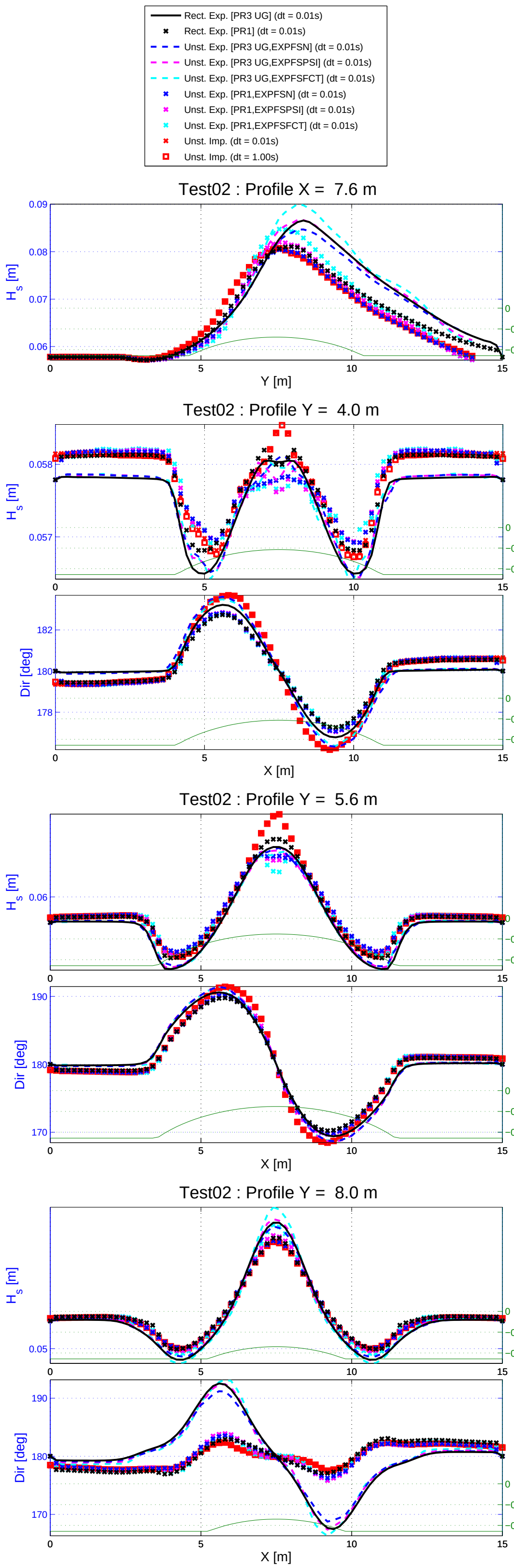

Figure 11: Profiles obtained after 40 seconds of integration for TEST02 (non-breaking case, narrow spectrum)

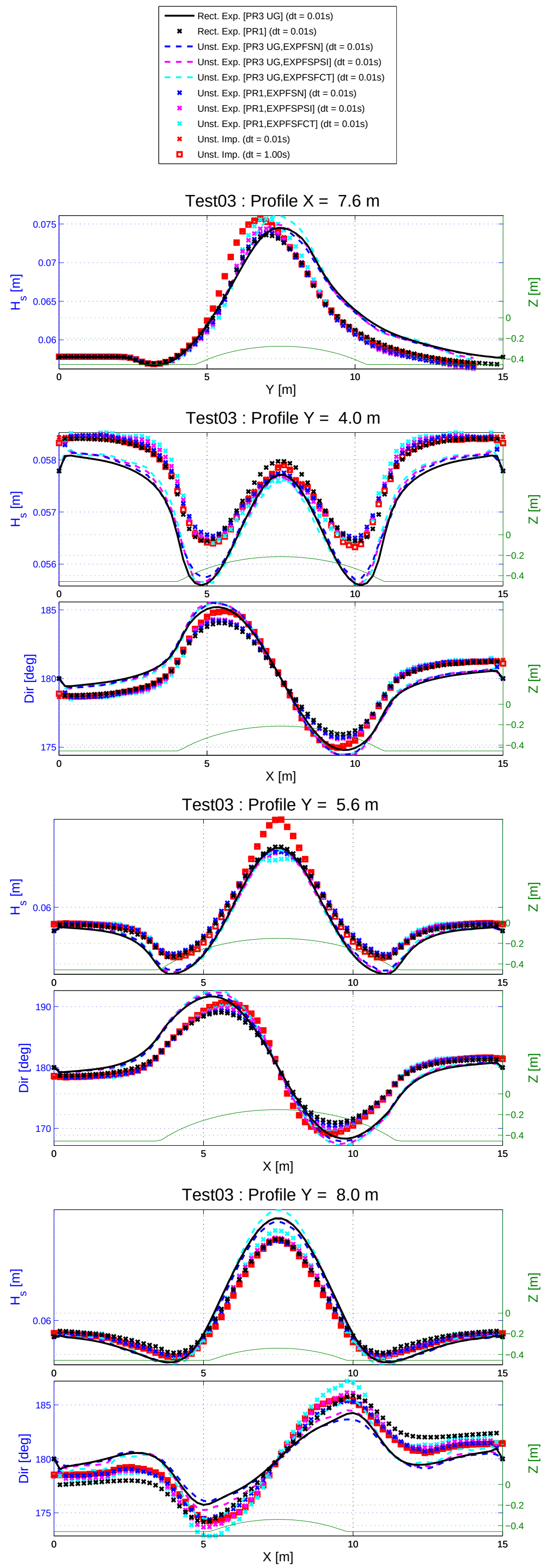

Figure 12: Profiles obtained after 40 seconds of integration for TEST03 (non-breaking case, broad spectrum)

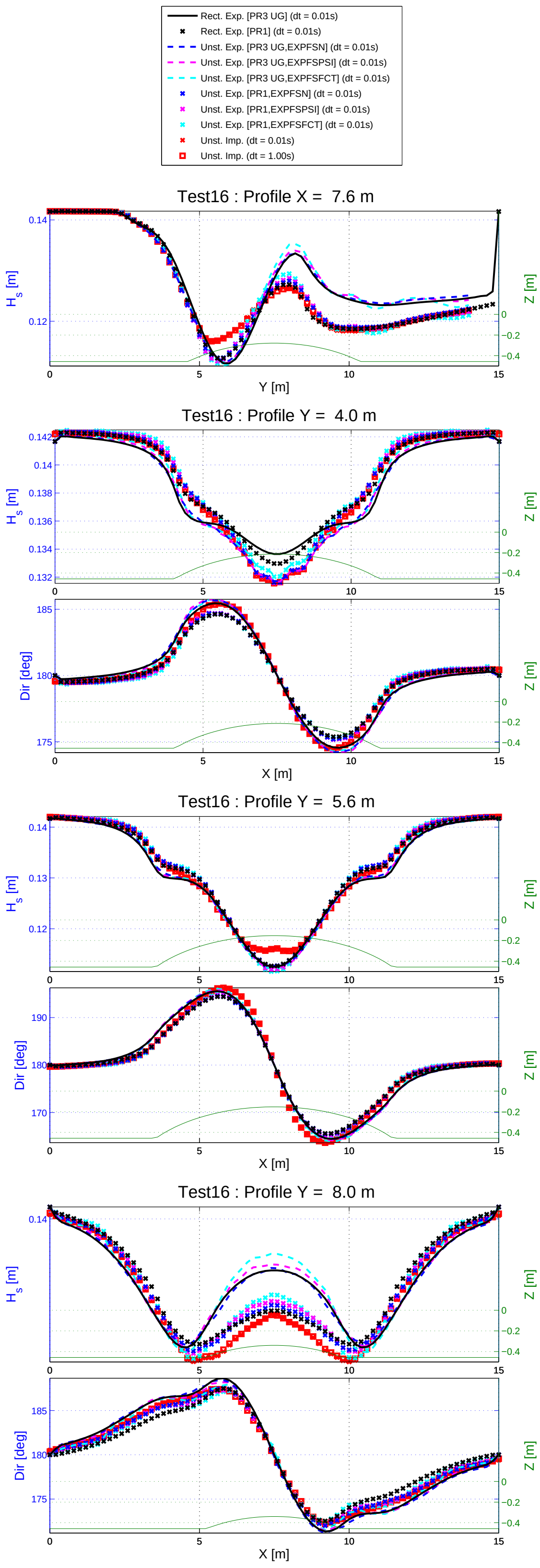

Figure 13: Profiles obtained after 40 seconds of integration for TEST16 (breaking case, broad spectrum)

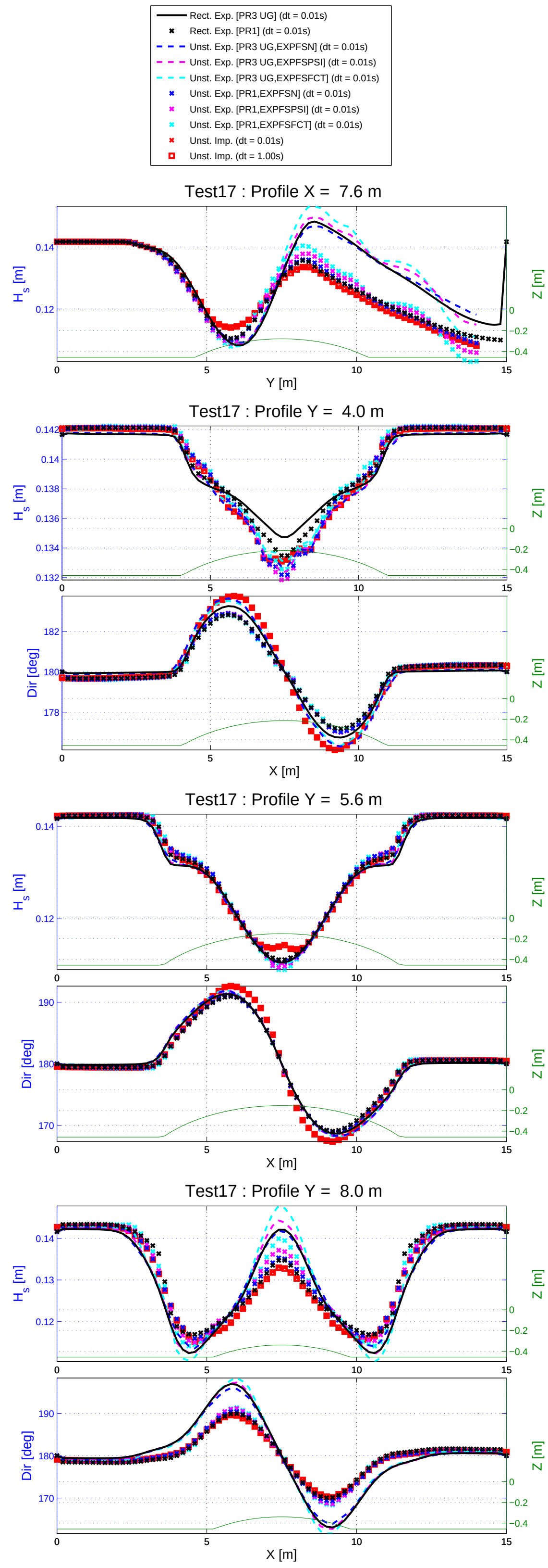

Figure 14: Profiles obtained after 40 seconds of integration for TEST17 (breaking case, narrow spectrum)

4 Implementation on the Iroise Sea

The real case is implemented on the Iroise Sea, at the west of Brittany, France. This sea provides both very strong tide currents and high tide water level variations. It is also scattered with many islands and rocky shoals. We here implemented an unstructured 12 518-node mesh represented in figure 15 [see Ardhuin et al., 2012]. This mesh was done using the POLYMESH tool. The open boundaries are forced by 121 forcing boundary nodes linearly spaced every 5 km. The coast line is resolved with a resolution of about 200 m.

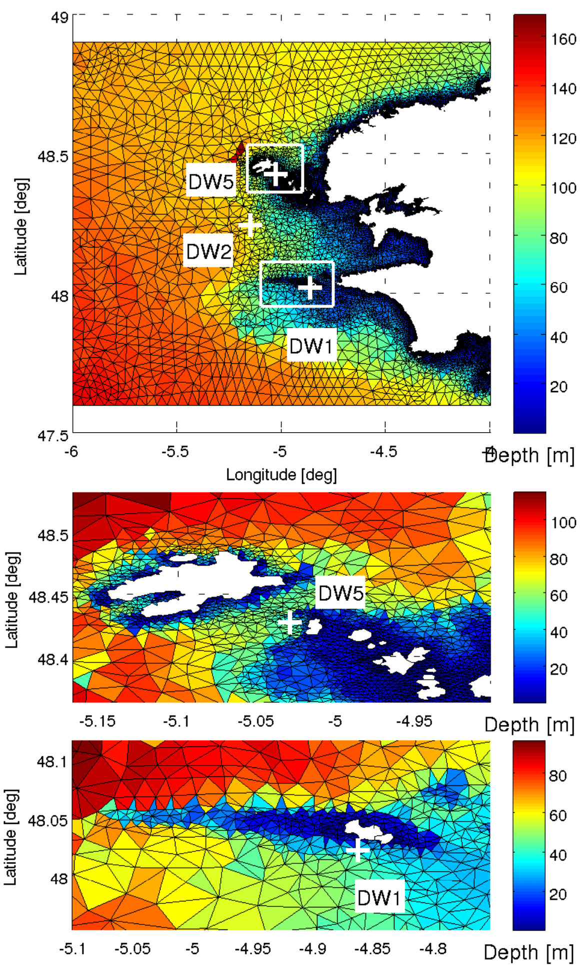

Figure 15: Unstructured mesh of the Iroise Sea implemented in WW3, from 5 km resolution offshore to about 200 m resolution at the coast line.

The boundary spectra are gotten from the PREVIMER/HOMERE WW3 hindcasts [Boudière et al., 2013] which provides 3-hour spectra close to each boundary point. The wind is obtained from the European Centre for Medium-Range Weather Forecast (ECMWF) hindcasts, with 1/4 degree space resolution and 3 hours time resolution. Finally, the water levels and the currents are obtained from PREVIMER MARS-2D hindcasts with 250 m space resolution and 15 minutes time resolution [see description in Ardhuin et al., 2012]. These forcing fields are then extrapolated on the mesh nodes. The hindcast presented here covers January and February, 2014. This period starts with a relative weak sea state in January, but with many successive storms in February, conjugated with high tides [Dodet et al., 2012]. Three DATAWELL recorded the wave field for this period at three interesting locations. A first DATAWELL (DW2) recorded data far from the islands and in a relatively smooth bathymetry area. A second DATAWELL (DW1) recorded data in the south of the Sein island. North-West incoming waves come to the buoy after crossing a rocky shoal at the west of the island. This shoal, named "Chaussée de Sein", is a shallow water area scattered with numerous rocks. Finally, a last DATAWELL (DW5) faces the West coast of Bannec island and is at the boarder of the "Fromveur" channel, where the tides provide strong currents, up to 4 m.s^{-1} in the channel, and up to 2 m.s^{-1} at the buoy location. The model is then integrated for the two months using the newly implemented full implicit scheme, with the physical parametrization TEST451 of Ardhuin et al. [2010].

At the DW2 location, over the full time series, the model slightly underestimates the significant wave height with a bias of -0.18 m. This bias is due to the difficulties of the model to reproduce the storm events. Indeed, when looking only at wave fields with a significant wave height inferior to 5 m, the model bias becomes 0.19 m, with a slight overestimation of the significant wave height. The RMS-Error is 0.43 m for the global time series, giving a normalized RMS-Error of 11.5%. This result comes directly from the good propagation of the waves forced at the boundary up to the buoy.

The next investigated buoy (DW5, figure 17) located next to the strong tide currents channel called "Fromveur" clearly shows the tidal variations of the waves, following the current and water level variations. The tidal variations are clearly visible on the significant wave height and the peak wave direction provided by the model. The amplitude of the peak wave direction variation is well in line with the observations, but the amplitude of the tidal variation of the wave height provided by the model is slightly understimated compared to the amplitude of the observed wave height tidal variations. The peak frequency time series provided by the model do not show the variability observed at the buoy. We also note that except for the storm event of February 14, 2015, the model globally overestimates the wave height. The bias is of 0.59 m with a RMSE of 0.73 m (N-RMSE = 23.8%). This error cumulates the slight general wave overestimation (except for storm events) at the western boundary that propagates to the buoy and the underestimation of the effects of the tidal currents and water levels on the wave height. These difficulties for the wave model to well reproduce the tidal variation may be due to an unaccurate withecapping dissipation term in presence of strong currents.

The DW1 buoy recorded wave parameters on the southern area of the Sein island. In that configuration the incoming prevailing swells (coming from West-North-West) must go over a large rocky shoal at the western extremity of the island. This shoal is sprinkled with a large number of small rocky clusters that block the waves. With the mesh used here, these rocky clusters are not resolved. As a result, the incoming waves are not sufficiently blocked by the shoal and the model provides a strong overestimation of the significant wave height compared to the buoy observations. With this king of strongly unsmoothed bathymetry, the need of high resolution meshes fastly resolved with the implicit scheme is highlight. Unfortunately, the results are not yet available.

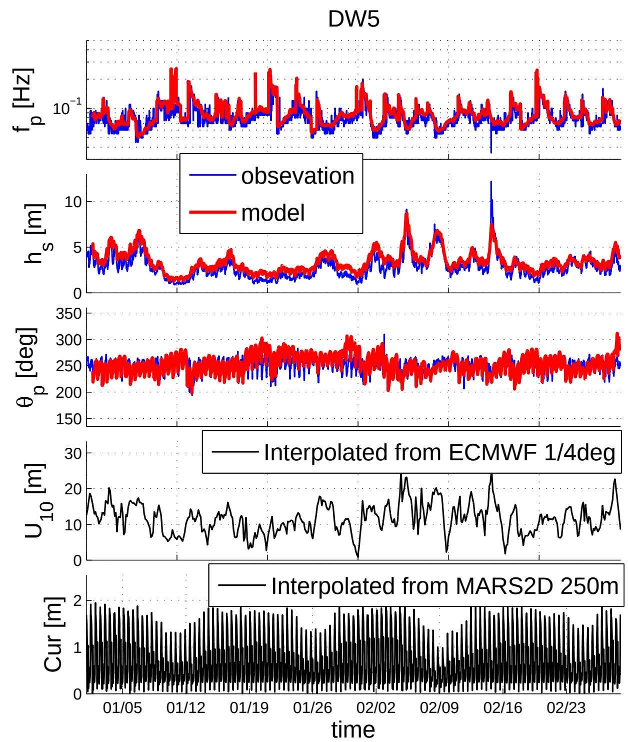

Figure 17: Comparison of wave buoy observations (DW5) with the implicit model hindcast results.

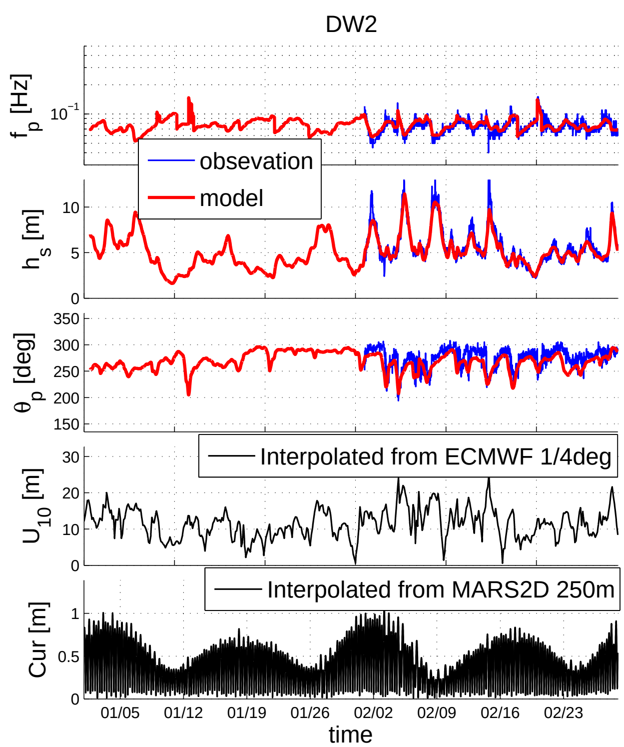

Figure 16: Comparison of wave buoy observations (DW2) with the implicit model hindcast results.

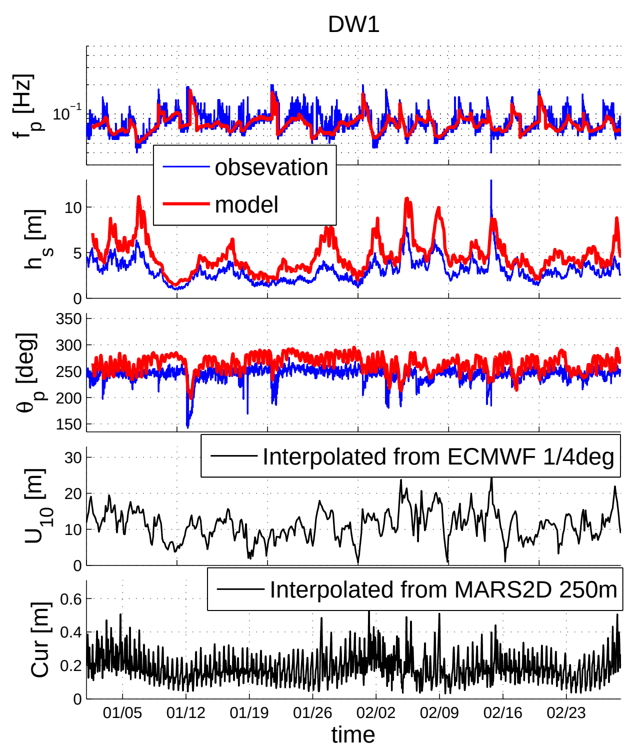

Figure 18: Comparison of wave buoy observations (DW1) with the implicit model hindcast results.

5 Conclusions

We have presented the verification of the numerical part and a 1st real case of a newly developed spectral wave model that was included in the WW3 framework and that is based on WWM-III. The model results are promising in terms of accuracy and efficiency. The next step will be to validate the full model for very high resolution bathymetries. Morever, we are thinking of a full validation test suite for unstructured grid models to have a evaluation of numerics in different environments. Since WWM-III was coupled to SCHISM Roland et al. [2012] the presented numerical framework is already well tested within a coupled wave current model in 2d and 3d. The numerical basis in the new wave model in WW3 also provides the basis for future REA (Rapid Environmental Assesment) and other activities that need fast and efficient downscaling. For explicit models, grids need to be carefully optimized in order to make the efficient integration possible. Fastly generated grids often have undesirable triangles that strongly reduce the time step, however in our method this does not pose a hard constraint. We are looking forward to extending this numerical basis for higher order non-linear methods and we are at this time developing a fully non-linear solver that will reduce further the time step dependency of the results and give the basis for the solution of extended version of the WAE that include higher order propagation effects.

Acknowlegments

We thank the technical group at the French Navy Hydrographic and Oceanographic Institute (SHOM) who deployed the buoys. This model development is part of the PREVIMER project co-funded by European Union, Ifremer, Brittany Region, Finistère departemental council and Brest Métropole Océane. This work was also supported by the research program PROTEVS funded by DGA and conducted by SHOM.

References

F. Ardhuin, B. Chapron, and F. Collard. Observation of swell dissipation across oceans. *Geophys. Res. Lett.*, 36:L06607, 2009. doi: 10.1029/2008GL037030.

F. Ardhuin, E. Rogers, A. Babanin, J.-F. Filipot, R. Magne, A. Roland, A. van der Westhuysen, P. Queffeulou, J.-M. Lefevre, L. Aouf, and F. Collard. Semi-empirical dissipation source functions for wind-wave models: part I, definition, calibration and validation. *J. Phys. Oceanogr.*, 40(9):1917–1941, 2010.

F. Ardhuin, A. Roland, F. Dumas, A.-C. Bennis, A. Sentchev, P. Forget, J. Wolf, F. Girard, P. Osuna, and M. Benoit. Numerical wave modeling in conditions with strong currents: Dissipation, refraction, and relative wind. *Journal of Physical Oceanography*, 42(12):2101–2120, 2012.

M. Benoit, F. Marcos, and F. Becq. Development of a third generation shallow-water wave model with unstructured spatial meshing. In *Proceedings of the 25th International Conference on Coastal Engineering, Orlando*, pages 465–478. ASCE, 1996.

E. Boudière, C. Maisondieu, F. Ardhuin, M. Accensi, L. Pineau-Guillou, and J. Lepesqueur. A suitable metocean hindcast database for the design of marine energy converters. *International Journal of Marine Energy*, 3, 2013.

J. Dietrich, M. Zijlema, P.-E. Allier, L. Holthuijsen, N. Booij, J. Meixner, J. Proft, C. Dawson, C. Bender, A. Naimaster, J. Smith, and J. Westerink. Limiters for spectral propagation velocities in swan, ocean modelling. *Ocean Modelling*, 70:85–102, 2013.

G. Dodet, S. Suanez, F. Leckler, F. Ardhuin, B. Fichaut, and R. Autret. Non-hydrostatic modelling of extreme water levels on banneg island, france. In *14th International Workshop on Wave Hindcasting and Forecasting, and 5th Coastal Hazard Symposium Key West, Florida, USA, Nov 8-13, 2015.*, 2012.

R. Gelci, H. Cazalé, and J. Vassal. Prévision de la houle. La méthode des densités spectroangulaires. *Bulletin d'information du Comité d'Océanographie et d'Etude des Côtes*, 9:416–435, 1957.

L. H. Holthuijsen, A. Herman, and N. Booij. Phase-decoupled refraction-diffraction for spectral wave models. *Coastal Eng.*, 49:291–305, 2003.

F. Leckler, F. Ardhuin, J.-F. Filipot, and A. Mironov. Dissipation source terms and whitecap statistics. *Ocean Modelling*, 70:62–74, 2013.

J.-M. Liau, A. Roland, T.-W. Hsu, S.-H. Ou, and Y.-T. Li. Wave refraction-diffraction effect in the wind wave model WWM. *Coastal Eng.*, 58:429–443, 2011.

S. Patankar. *Numerical heat transfer and fluid flow: Computational methods in mechanics and thermal science.* Hemisphere Publishing Corp., Washington, DC, 1980.

A. Roland. *Development of WWM II: Spectral wave modelling on unstructured meshes.* PhD thesis, Technische Universität Darmstadt, Institute of Hydraulic and Water Resources Engineering, 2008.

A. Roland and F. Ardhuin. On the developments of spectral wave models: numerics and parameterizations for the coastal ocean. *Ocean Dynamics*, 64(6):833–846, 2014.

A. Roland, P. Mewis, U. Zanke, S. Ou, T. Hsu, and J. Liau. Verification and improvement of a spectral finite element wave model. In *Proceedings of the 5th International Symposium Ocean Wave Measurement and Analysis, Madrid, june 2005.* ASCE, 2005. Paper number 157.

A. Roland, Y. J. Zhang, H. V. Wang, Y. Meng, Y.-C. Teng, V. Maderich, I. Brovchenko, M. Dutour-Sikiric, and U. Zanke. A fully coupled 3d wave-current interaction model on unstructured grids. *Journal of Geophysical Research: Oceans (1978–2012)*, 117(C11), 2012.

Y. Toledo, T.-W. Hsu, and A. Roland. Extended time-dependent mild-slope and wave-action equations for wave-bottom and wave-current interactions. *Proc. Roy. Soc. Lond. A*, 468:184–205, 2012. doi: 10.1098/rspa.2011.037.

H. Tolman, M. Accensi, H. Alves, F. Ardhuin, J. Bidlot, N. Booij, A.-C. Bennis, T. Campbell, D. V. Chalikov, J.-F. Filipot, et al. User manual and system documentation of wavewatch iii version 4.18. 2014.

C. L. Vincent and M. J. Briggs. Refraction-diffraction of irregular waves over a mound. *Journal of Waterway, Port, Coastal, and Ocean Engineering*, 115(2):269–284, 1989.

WISE Group. Wave modelling - the state of the art. *Progress in Oceanography*, 75:603–674, 2007. doi: 10.1016/j.pocean.2007.05.005.